

Impacts of TROPOMI-Derived NO_x Emissions on NO₂ and O₃ Simulations in the NCP during COVID-19

Yizhi Zhu, Cheng Liu,* Qihou Hu,* Jiahua Teng, Daian You, Chengxin Zhang, Jinping Ou, Ting Liu, Jinan Lin, Tianyi Xu, and Xinhua Hong



Cite This: *ACS Environ. Au* 2022, 2, 441–454



Read Online

ACCESS |

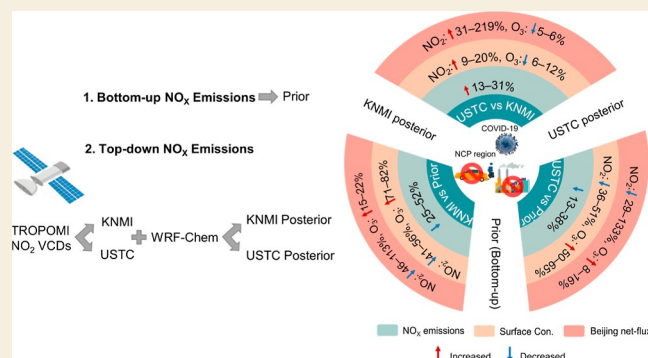
Metrics & More

Article Recommendations

Supporting Information

ABSTRACT: NO₂ and O₃ simulations have great uncertainties during the COVID-19 epidemic, but their biases and spatial distributions can be improved with NO₂ assimilations. This study adopted two top-down NO_x inversions and estimated their impacts on NO₂ and O₃ simulation for three periods: the normal operation period (P1), the epidemic lockdown period following the Spring Festival (P2), and back to work period (P3) in the North China Plain (NCP). Two Tropospheric Monitoring Instrument (TROPOMI) NO₂ retrievals came from the Royal Netherlands Meteorological Institute (KNMI) and the University of Science and Technology of China (USTC), respectively. Compared to the prior NO_x emissions, the two TROPOMI posteriors greatly reduced the biases between simulations with in situ measurements (NO₂ MREs: prior 85%, KNMI −27%, USTC −15%; O₃ MREs: Prior −39%, KNMI 18%, USTC 11%). The NO_x budgets from the USTC posterior were 17–31% higher than those from the KNMI one. Consequently, surface NO₂ levels constrained by USTC-TROPOMI were 9–20% higher than those by the KNMI one, and O₃ is 6–12% lower. Moreover, USTC posterior simulations showed more significant changes in adjacent periods (surface NO₂: P2 vs P1, −46%, P3 vs P2, +25%; surface O₃: P2 vs P1, +75%, P3 vs P2, +18%) than the KNMI one. For the transport flux in Beijing (BJ), the O₃ flux differed by 5–6% between the two posterior simulations, but the difference of NO₂ flux between P2 and P3 was significant, where the USTC posterior NO₂ flux was 1.5–2 times higher than the KNMI one. Overall, our results highlight the discrepancies in NO₂ and O₃ simulations constrained by two TROPOMI products and demonstrate that the USTC posterior has lower bias in the NCP during COVID-19.

KEYWORDS: TROPOMI NO₂, top-down NO_x emissions, WRF-Chem model, North China Plain, O₃ concentration, transport flux



1. INTRODUCTION

NO_x (NO_x = NO₂ + NO) emissions made great contributions to the severe air pollution in the region. High levels of NO_x emissions lead to atmospheric significant nitrogen deposition in terrestrial and aquatic ecosystems throughout East Asia.^{1,2} NO_x can also react with volatile organic compounds (VOCs) and so forth to form ozone (O₃),^{3–8} which is another important gas pollutant and also harmful to the respiratory system, air quality, climate, and the biosphere.⁹

Previous studies have demonstrated that the magnitude of O₃ changes to unit changes in precursors varies in a complex non-linear fashion.^{4,10,11} For instance, despite the widespread decrease of NO_x emissions across the United States, observed O₃ trends are heterogeneous in space and time: decreasing in summer over less urbanized areas, and increasing in winter, night, and urban cores.^{12–14} Studied the relationship between NO_x and O₃ through air quality model was a convenient method.¹⁵ NO_x emissions can affect O₃ simulation through tropospheric chemistry has been confirmed in many studies.^{16,17}

Considering the importance of NO_x for the simulations of O₃ and relevant tracers,^{18,19} Quantifying NO_x emissions was the key part and first step of the atmospheric chemical-transport model simulation. On the traditional way, NO_x inventories were developed using a bottom-up method.²⁰ Because the bottom-up NO_x emissions are easily phased out quickly due to both rapid anthropogenic emissions changes, and fast response of NO₂ to its emissions resulting from the relatively short life time of NO₂ (3 h to 2 days).²¹ One way to improve the NO_x emission is to use observations to constrain bottom-up emissions. In this procedure, emissions are optimized in order to reduce differences between simulations and observations (e.g., surface, aircraft, and satellite remote

Received: March 17, 2022

Revised: June 22, 2022

Accepted: June 22, 2022

Published: July 5, 2022



Table 1. NO₂ Retrieval Settings Used in the KNMI and USTC Algorithms

NO ₂ retrieval settings for TROPOMI		KNMI	USTC
SCD retrievals		TROPOMI NO ₂ processor ³⁹	QDOAS
calculation of NO ₂ AMF	RTM	doubling-adding KNMI (DAK) radiative transfer model, version 3.2 ⁵²	vector linearized discrete ordinate radiative transfer model (VLIDORT), version 2.7 ⁴⁶
	method	look-up table (LUT) interpolation ⁵²	pixel-by-pixel calculation
	a priori NO ₂ vertical profiles	data assimilation/chemistry transport model version 5 (TMS-MP); spatial resolution: 1° × 1° ⁵³	WRF-Chem version 4.0; Spatial resolution: 20 km × 20 km ³⁴
stratosphere–troposphere separation of NO ₂		TMS-MP ^{52,53}	STREAM ⁴⁹

sensing).^{22–25} Among the types of observed data, updating NO_x inventories using satellite measurements is an effective technique and has been addressed in many studies.^{26–29}

Because satellites can provide high spatial resolution and wide spatial–temporal coverage. The shutdown of the China socioeconomic activities during the COVID-19 provides an opportunity to investigate the response of NO₂ and O₃ to the abrupt NO_x emission reductions.³⁰ Zhang et al.³¹ found that TROPOMI-derived NO_x emission in the lockdown period is 53.4% lower than the same period in 2019, leads to 36.5% O₃ increase and 12.5% PM_{2.5} decrease over East China.

Nonetheless, NO_x emissions constrained by different satellite retrievals may have an obvious discrepancy.³² The magnitude of tropospheric NO₂ column densities from two global retrievals from the National Aeronautics and Space Administration (NASA) and the KNMI differ by 50% and show different trends at the regional scale.³³ These differences in column densities can propagate to differences in the estimated top-down NO_x emissions. Qu et al.¹⁷ performed global inversions of NO_x emissions from 2005 to 2016 using two widely used OMI NO₂ retrievals from NASA (OMNO2 v3) and KNMI (DOMINO v2). The DOMINO posterior NO_x emissions have larger magnitudes than the prior and NASA posterior emissions.

Here, we investigate the importance of these discrepancies in NO_x emissions for the simulation of O₃ during COVID-19. We derived regional top-down NO_x emissions using two NO₂ products (KNMI and USTC) retrieved from TROPOMI. Then, we assessed their ability to reproduce real concentrations of NO₂ and O₃ by comparing the simulations with surface measurements from the multi-axis differential optical absorption spectroscopy (MAX-DOAS) instrument and the China National Environmental Monitoring Center (CNEMC) network. We also analyzed the different response of NO₂ and O₃ concentrations to large changes in NO_x emissions over the three periods: P1 (1 January to 22 January 2020), P2 (23 January to 17 February 2020), and P3 (18 February to 31 March 2020). Finally, the discrepancy in the transport flux of NO₂ and O₃ in Beijing (BJ) using different NO_x emissions was evaluated. Section 2 describes the Weather Research and Forecasting with coupled chemistry model (WRF-Chem) setting, TROPOMI NO₂ retrieval, top-down NO_x emissions adjustment methods, MAX-DOAS NO₂ retrieval methods, and transport flux calculation; Section 3 discusses the differences in NO₂ and O₃ levels, trends, and transport fluxes, which are influenced by changes in NO_x emissions; and Section 4 presents the conclusions of this study.

2. METHODS

2.1. WRF-Chem Simulation

WRF-Chem model simulation was used to derive the NO_x emissions estimates in NCP at 20 × 20 km resolution and obtain the distribution of air pollutants. The simulation domain covered the NCP region (32°N–44°N, 108°E–124°E), with a center point of 38.0°N, 115.6°E from January to March 2020. The physical and chemical configurations adopted in this study have been described in.³⁴ The 6 h final operational global analysis (FNL) data (<https://rda.ucar.edu/datasets/ds083.2/index.html>, last access: 12 June 2020) were obtained from the National Centers for Environmental Prediction (NCEP), which provide the initial meteorological fields and boundary conditions. To reproduce the meteorology accurately, the weather data for observation nudging are obtained from the NCEP Administrative Data Processing (ADP) Global Surface Observational Weather data (ds461.0) (<https://rda.ucar.edu/datasets/ds461.0/>, last access: 27 June 2020) and Upper Air Observational Weather data (ds351.0) (<https://rda.ucar.edu/datasets/ds351.0/index.html>, last access: 27 June 2020). The Carbon-Bond Mechanism version Z photochemical mechanism³⁵ combined with the Model for Simulating Aerosol Interactions and Chemistry³⁶ was used to simulate the chemical process in the atmosphere. The bottom-up anthropogenic emissions data were acquired from the MEIC in 2017 developed by Tsinghua University (<http://meicmodel.org/>, last access: 16 November 2020). The fire inventory of National Center for Atmospheric Research (NCAR) was the data source for the near-real-time fire emissions, which are based on moderate resolution imaging spectroradiometer rapid response fire counts (<https://www.acom.ucar.edu/acresp/forecast/fire-emissions.shtml>, last access: 17 November 2020). The biogenic emissions were calculated online using the Model of Emissions of Gases and Aerosols from Nature (<https://www2.acom.ucar.edu/modeling/model-emissions-gases-and-aerosols-nature-megan>, last access: 17 November 2020) embedded in the WRF-Chem model.

2.2. TROPOMI NO₂ Retrieval

TROPOMI, on-board the Sentinel-5 Precursor satellite, is a nadir-viewing hyperspectral spectrometer launched on 13 October 2017 by the European Space Agency (ESA). TROPOMI images capture various air pollutants in UV–visible–near-infrared spectra at 13:30 local time each day with a fine spatial resolution of 7 × 3.5 km² at nadir (increased to 5.5 × 3.5 km² since August 2019).^{37,38} Two level-2 NO₂ retrieval products are used to derive the regional top-down NO_x emissions in this study: the operational KNMI and USTC products. NO₂ retrieval algorithm information of the former has been described in detail by.³⁹ The latter followed the satellite trace gas retrieval algorithms from USTC.^{40–43} The TropNO₂VCDs retrieval consists of three steps: (1) spectral fitting of total NO₂ slant column densities (SCDs), SCD_{total}; (2) Air mass factor (AMF) calculation, AMF_{strat} and AMF_{tropo}; (3) Separate stratospheric NO₂ contribution from total NO₂ column. Therefore, the TropNO₂VCDs (VCD_{strat}) can be computed by the following equation

$$\text{VCD}_{\text{strat}} = \frac{\text{SCD}_{\text{total}} - \text{AMF}_{\text{strat}} \times \text{VCD}_{\text{strat}}}{\text{AMF}_{\text{tropo}}}$$

For the total NO₂ SCD retrieval, the wavelength range of 405–465 nm was selected for spectral fitting with the QDOAS software.⁴⁴ QDOAS is based on nonlinear least square method and is configured to follow the recommendations in the QA4ECV NO₂ project.⁴⁵ For the AMFs in the troposphere and stratosphere, Vector Linearized Discrete Ordinate Radiative Transfer (VLIDORT) model version 2.7⁴⁶ and a priori NO₂ vertical profiles were utilized. Using accurate and high-resolution data (spatially and temporally) as inputs in calculating the AMF can significantly reduce the overall errors of the AMF and thus the tropospheric vertical column content.^{47,48} In this study, the local-updated NO₂ vertical profiles with a horizontal resolution of 20 km × 20 km was provided by WRF-Chem simulation.³⁴ In order to separate the contribution of stratospheric NO₂ from the total NO₂ column, the Stratospheric Estimation Algorithm from Mainz (STREAM)⁴⁹ was used in this study. The details for the two NO₂ retrieval settings are listed in Table 1. Note that satellite pixels were filtered out first if satisfying any of the following rejection criteria: cloud radiance fraction larger than 30%; root mean square (RMS) of the spectral fitting larger than 0.002; pixels affected by the row anomaly; solar zenith angle larger than 70°; and other quality flags.⁵⁰ For the tropospheric NO₂ vertical column densities (TropNO₂VCDs) in NO_x emissions estimation, a novel P-spline method⁵¹ was used to re-grid NO₂ VCDs into a level-3 product with a resolution of 20 km × 20 km.

2.3. Top-Down NO_x Emissions

For this study, the mass balance procedure developed by Martin²¹ and improved by Lamsal et al.⁵⁴ and Vinken et al.⁵⁵ was used to estimate the top-down NO_x emissions. This method considered the fact that TropNO₂VCDs respond non-linearly to surface NO_x emission change. We performed a sensitivity study by perturbing surface NO_x emission by 20% to get the scaling factor β, which denotes the relative change of simulated TropNO₂VCDs due to a 1% change in NO_x emission. We also take into account the dimensionless factor (γ) following Visser et al.,¹⁶ which reflects the influence of NO_x emission on the tropospheric AMF calculation. The equation used to estimate the top-down NO_x emission (E_{td}) based on bottom-up NO_x emission (E_{bu}), TROPOMI TropNO₂VCDs with AMF from WRF-Chem using bottom-up NO_x emission (C_{TROPOMI_m, bu}) and simulated TropNO₂VCDs using bottom-up NO_x emission (C_{m, bu}) is as follows

$$E_{td} = E_{bu}(1 + \beta(1 + \gamma)) \frac{C_{TROPOMI_m, bu} - C_{m, bu}}{C_{m, bu}}$$

The scale factors β and γ are calculated using the following equations

$$\beta = \frac{20\%}{(C_{m, 1.2bu} - C_{m, bu}) / C_{m, bu}}$$

$$\gamma = \frac{(C_{TROPOMI_m, 1.2bu} - C_{TROPOMI_m, bu}) / C_{TROPOMI_m, bu}}{(C_{m, 1.2bu} - C_{m, bu}) / C_{m, bu}}$$

Uncertainties in the NO_x emissions are mostly driven by the TROPOMI NO₂ retrieval errors and the error of linking local NO₂ VCDs to local emissions on the basis of model simulations. The latter was estimated at ~30% by Zhao and Wang⁵⁶ and Lorente et al.⁵⁷ TROPOMI NO₂ retrieval errors mainly from the computation of AMFs. We compared the TROPOMI TropNO₂VCDs to MAX-DOAS measurements (Figure 5). The mean of relative errors < 30% (KNMI: 29%, USTC: 22%). Therefore, the total error estimations are ~42 and ~37% for KNMI and USTC posterior NO_x emissions, respectively. This is similar to the uncertainty estimate for the mass balance approach for single determinations, reported by Cambaliza et al.⁵⁸

2.4. MAX-DOAS Measurements

Three MAX-DOAS instruments were positioned in the southwest of BJ at the following sites: WD (115.15°N, 38.17°E), QKY (39.95°N, 116.32°E), and DQS (39.98°N, 116.38°E). This compact instrument consists of an ultraviolet spectrometer with a scanning telescope, a

stepping motor acting as a controlling unit on the viewing zenith angle of the telescope, and a spectrometer covering the visible (Vis) wavelength range from 393 to 525 nm. The scattered sunlight collected by the telescope was redirected by a prism reflector to the spectrometer for spectral analysis. The viewing azimuth angle (θ) of the telescope was adjusted to 195° with a lowest elevation angle of 3°. A measurement sequence consisted of measuring scattered sunlight spectra at elevation angles (α) of 90° (zenith), 30, 15, 10, 7, 5, and 3°. To achieve similar intensity levels for all the measurements, the number of scans and exposure time for each measurement were adjusted automatically depending on the intensity of received scattered sunlight. A complete measurement sequence required approximately 4 min depending on the measured intensity. All measured spectra were first corrected for offset and dark current. The Fraunhofer reference was used to remove the solar Fraunhofer structure in the scattered sunlight, which was usually selected at the 90° elevation angle during noon on a clear day. The spectra evaluation software QDOAS developed by BIRA-IASB (<http://uv-vis.aeronomie.be/software/QDOAS/>) was used for the spectral fitting analysis. The detailed configuration of the spectral fitting is listed in ref 42. The fitting wavelength interval of NO₂ was 338–370 nm, and trace gas absorption cross sections of NO₂ were included at 220 and 298 K in the fitting. The DOAS spectral retrieval results are the differential slant column densities (DSCDs), which are defined as the difference between the SCD of the measured spectrum and the Fraunhofer reference spectrum. The AMF⁵⁹ was applied to convert the DSCDs into VCDs to compare the measurements with each other. Because the DOAS analysis results were the DSCDs, we applied the concept of differential air mass factor (DAMF) to convert the measurements to VCDs as follows (α: denotes the elevation angle and α ≠ 90°)

$$DAMF_{\alpha} = AMF_{\alpha} - AMF_{90} \quad (1)$$

The tropospheric DSCD_α can be expressed as

$$DSCD_{\alpha} = SCD_{\alpha} - SCD_{90} \quad (2)$$

The VCD was calculated with AMF as

$$VCD = SCD / AMF \quad (3)$$

$$SCD_{\alpha} = VCD \cdot AMF_{\alpha} \quad (4)$$

$$SCD_{90} = VCD \cdot AMF_{90} \quad (5)$$

By substituting eqs 4 and 5 into eq 2, and applying eq 1, we obtained the final value as

$$VCD = DSCD_{\alpha} / DAMF_{\alpha} \quad (6)$$

2.5. Inter-Cities Boundary Transport

The transport flux here represent the mass of air pollutant that passes through a vertical plane over a period of time.⁶⁰ In this study, we calculated the fluxes of NO₂ and O₃ at the administrative boundary of the BJ in the three periods. According to previous studies,^{61,62} the inter-city transport flux was calculated as follows, the example of flux calculation is shown in Figure S1.

$$\text{Flux} = \sum_{i=1}^n \sum_l H_i x c w \cdot v$$

where l is the length of administrative boundary line, which is numerically equal to the product of grid resolution and the number of boundary grids; n is the number of layers from the ground to tropopause; H_i is the height between layer i and i + 1; x is the grid width; c is the averaged concentration of NO₂ or O₃ at the vertical grid cell; w is the wind vector; and v is the normal vector of the vertical grid cell. The variables in the expression can be obtained from the WRF-Chem simulation. Fluxes through the vertical plane that flow out of BJ is considered outflow fluxes and treated as positive. Conversely, the flux flow into BJ is considered inflow fluxes and are treated as negative. The net flux of the BJ is the sum of inflowing and outflowing fluxes.

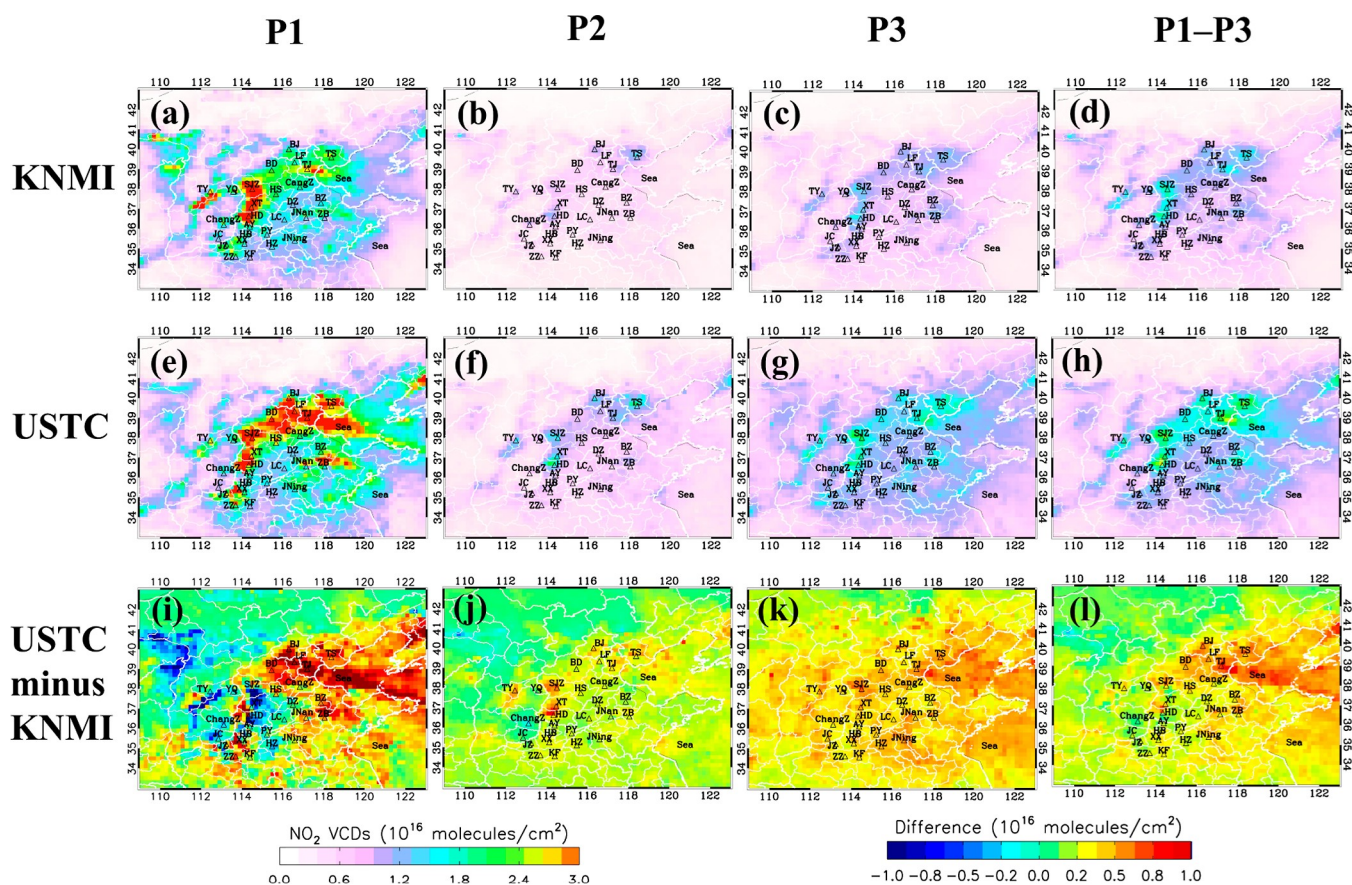


Figure 1. TROPOMI TropNO₂VCDs and their differences (USTC minus KNMI) for P1 (a,e,i), P2 (b,f,j), P3 (c,g,k), and the average of three-period (d,h,l). Note: (BJ: Beijing, TJ: Tianjin, SJZ: Shijiazhuang, TS: Tangshan, BD: Baoding, LF: Langfang, CangZ: Cangzhou, HS: Hengshui, HD: Handan, XT: Xingtai, TY: Taiyuan, YQ: Yangquan, ChangZ: Changzhi, JC: Jincheng, JNan: Jinan, ZB: Zibo, LC: Liaocheng, DZ: Dezhou, BZ: Binzhou, JNing: Jining, HZ: Heze, ZZ: Zhengzhou, XX: Xinxiang, HB: Hebi, AY: Anyang, JZ: Jiaozuo, PY: Puyang, and KF: Kaifeng.)

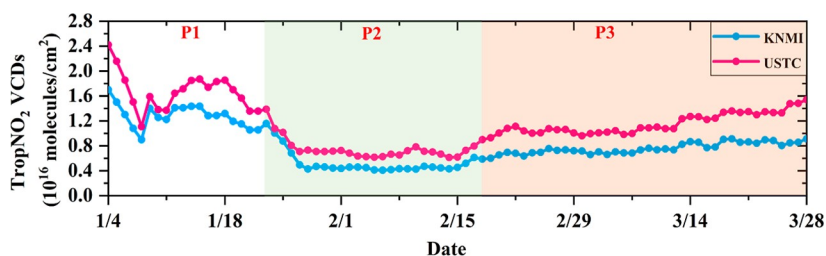


Figure 2. Evolution of the mean concentration of TropNO₂VCDs observed by the satellites in “2 + 26” cities during the three periods. Note: the time series with daily variation is a 7-day moving average.

2.6. Ancillary Data

We evaluated the surface simulations of NO₂ and O₃ with hourly measurements from the CNEMC network (<http://www.cnemc.cn/en/>, last access: 28 July 2020). The 0–23 h concentrations of these measurements from January to March 2020 were used in this study. For this study, 152 in situ sites over “2 + 26” cities are taken into account. Data quality control has been applied to the CNEMC measurements to remove unreliable outliers following previous study.⁶³

3. RESULTS

3.1. Magnitude and Trend of TROPOMI NO₂

The Ministry of Environmental Protection in China released the Air Pollution Prevention and Control Work Plan in February 2017, which referred to the cities that transmit air pollution as “2 + 26” cities (represented by triangles in Figure

1) for the first time. The “2 + 26” cities represent 28 NO_x polluted cities in the NCP, including 2 cities with significant NO_x pollution [BJ and Tianjin (TJ)] and 26 cities (the rest of the cities) with high NO_x concentrations.

In “2 + 26” cities, the KNMI TropNO₂VCDs (Figure 1a–c) were 1.28, 0.58, and 0.76 × 10¹⁶ molecules/cm² during P1, P2, and P3, and the USTC TropNO₂VCDs (Figure 1e–g) were 1.68, 0.73, and 1.16 × 10¹⁶ molecules/cm², respectively. The TropNO₂VCDs from USTC were 31, 26, and 53% higher than those from KNMI; the averaged TropNO₂VCDs for the three periods for USTC were 42% higher than those for KNMI. This phenomenon also has been identified previously, which the current TROPOMI operational NO₂ product may have a low bias of 20–40% in urban areas.^{64,65} Compared with P1, the TropNO₂VCDs for P2 had decreased by 55% for the KNMI products and by 57% for the USTC products. In contrast,

compared with P2, the TropNO₂VCDs for P3 had increased by 31% for the KNMI product and by 59% for the USTC product (Figure 2). Compared to the USTC retrieval, the KNMI captured significantly decreased in TropNO₂VCDs from P1 to P2, while had little sign of recovery in P3. Figure 3

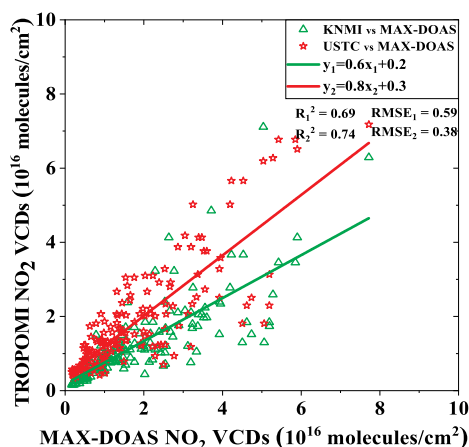


Figure 3. Scatterplot of TROPOMI [KNMI (green), USTC (red)] and MAX-DOAS observed TropNO₂VCDs.

indicated that the two TropNO₂VCD retrievals are both in good agreement with MAX-DOAS observation (R^2 : KNMI 0.69, USTC 0.74), and the USTC products have a smaller mean square error (RMSE: KNMI 0.59, USTC 0.38). Additionally, the TropNO₂VCDs showed significant spatial disparities in the three periods. To better demonstrate the response of provincial-level pollutants to Chinese government policies, we divide “2 + 26” cities into six provinces: BJ, TJ, Hebei (HB, include Shijiazhuang, Tangshan, Langfang, Baoding, Cangzhou, Hengshui, Xingtai, and Handan), Henan (HN, include Zhengzhou, Kaifeng, Anyang, Hebi, Xinxiang, Jiaozuo, and Puyang), Shanxi (SX, include Taiyuan, Yangquan, Changzhi, and Jincheng), and Shandong (SD, Jinan, Zibo, Jining, Dezhou, Liaocheng, Binzhou, and Heze). From the provincial differences, BJ, TJ, and cities in HB had higher values of TropNO₂VCDs during P1. From P1 to P2, the most rapid decline in TropNO₂VCDs also occurred in these three regions. In China, most of China’s production capacity is concentrated there. Moreover, the governments in these areas are more open than other regions,⁶⁶ so they were able to more quickly respond to the emergency measures. Therefore, enterprises in these regions were more affected by the epidemic, resulting in more significant changes in NO_x emissions and concentrations.

3.2. Estimation of NO_x Emissions

Discrepancy in NO₂ retrieval products is a major source of uncertainties in the top-down NO_x emission estimations. The different vertical sensitivities in the two NO₂ retrievals affect both magnitude and variations of top-down NO_x emissions. As shown in Table 2, the USTC posterior NO_x emissions had a larger magnitude than the KNMI posterior one. The budgets of the three-period averaged NO_x emissions from the KNMI posterior emissions in the six provinces were approximately 18–49% lower than the prior emissions; the USTC posterior emissions were approximately 4–35% lower than the prior emissions; and the USTC posterior emissions were approximately 17–31% higher than the KNMI posterior emissions. The largest difference between the two posterior emissions was in TJ, where the USTC values were 31% higher than those for KNMI; the USTC values were approximately 20% higher than those for KNMI in the remaining five provinces.

In terms of the different periods (Table S1), the prior (bottom-up) NO_x emissions remained unchanged during P2 when compared to P1, whereas significant reductions were observed after satellite adjustments [the KNMI and USTC posterior decreased by 16–51% (averaged –27%) and 18–54% (averaged –34%) respectively]. Prior (MEIC) NO_x emissions in most provinces barely changed (except BJ and TJ, which declined slightly by 15 and 7% respectively) from P2 to P3, whereas the emissions increased significantly after satellite constraints [KNMI and USTC posterior increased by 10–44% (averaged +30%) and 34–71% (averaged +50%) respectively]. This implies that, compared with the bottom-up inventory, the top-down NO_x inventory are better able to reflect the lockdown and recovery of human activity in a timely manner.⁶⁷

3.3. NO_x Emission Evaluation

To evaluate the magnitude of the prior and posterior NO_x emissions, we compared the simulations of surface NO₂ and O₃ concentrations using the prior, KNMI posterior, and USTC posterior NO_x emissions with surface measurements.

3.3.1. Comparison between Simulated Surface Concentrations and In Situ Observation. In “2 + 26” cities, the correlation between simulations and CNEMC data was significantly improved after top-down adjustments (Figure 4), and the R^2 values of NO₂ and O₃ simulated from prior NO_x emissions were 0.58 and 0.60, respectively. After the top-down adjustment in NO_x emissions, the R^2 of NO₂ increased to 0.69 (KNMI posterior) and 0.78 (USTC posterior), and the R^2 of O₃ increased to 0.67 (KNMI posterior) and 0.74 (USTC posterior); the mean relative errors (MREs) for NO₂ concentrations decreased from 85 to –27% (KNMI posterior) and –15% (USTC posterior); the MREs for O₃ concentrations decreased from –39 to 18% (KNMI posterior) and 11% (USTC posterior). WRF-Chem simulations using the USTC

Table 2. NO_x Emissions Budgets in the “2 + 26” Cities during Jan.–Mar., 2020 (Gg/month)

region	prior	KNMI posterior	USTC posterior	KNMI posterior vs prior (%)	USTC posterior vs prior (%)	USTC posterior vs KNMI posterior (%)
Beijing	13	7	8	–46	–35	20
Tianjin	16	8	10	–49	–34	31
Hebei	61	39	46	–36	–24	18
Henan	23	15	18	–36	–24	19
Shaanxi	16	13	15	–18	–4	17
Shandong	39	27	32	–32	–19	20

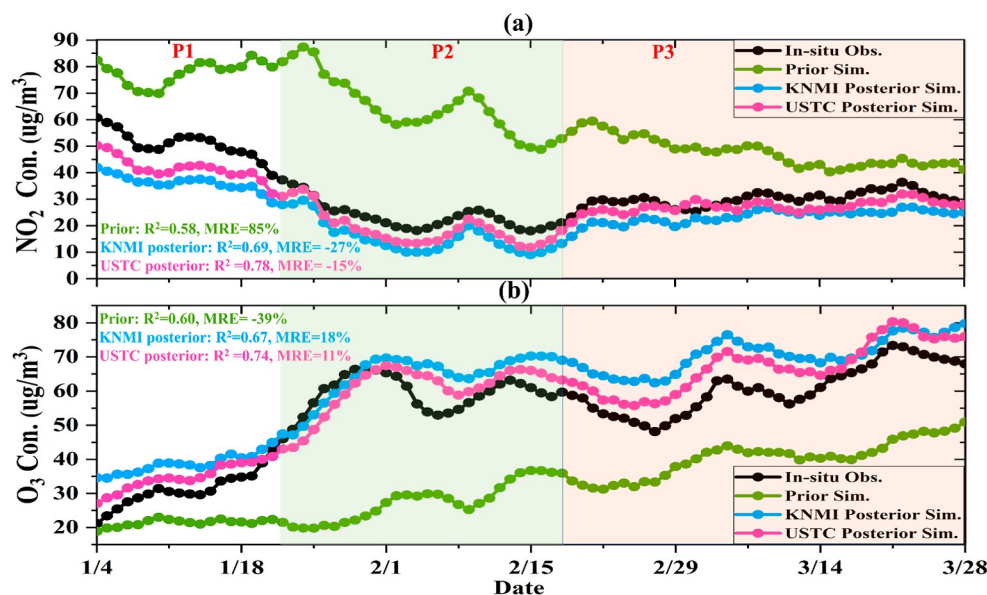


Figure 4. Comparison of simulation and CNEMC measurements during COVID-19. The time series concentrations of (a) NO₂ and (b) O₃ are 0–23 h averaged from 152 in situ sites over “2 + 26” cities. Note: Con., concentration, Obs., observed, and Sim., simulated.

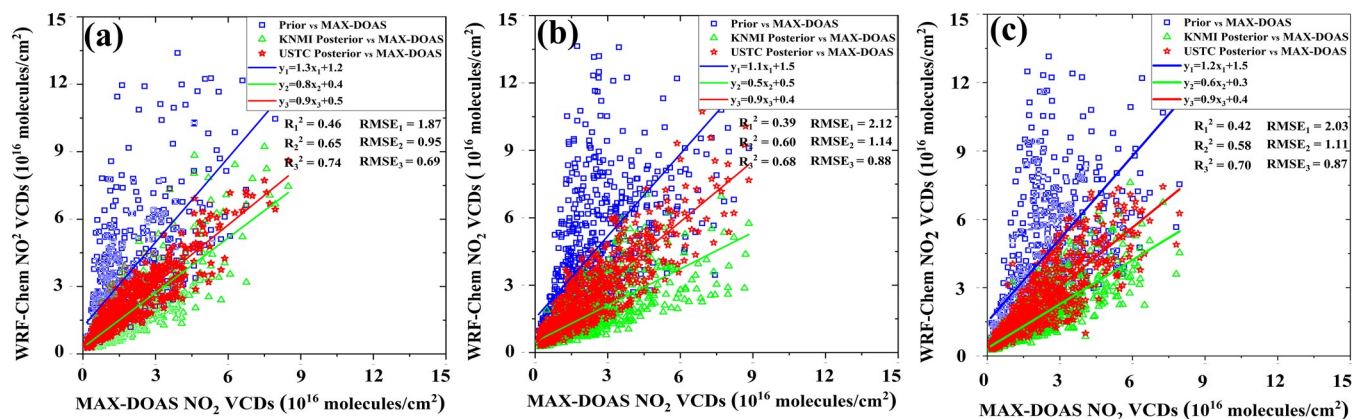


Figure 5. Evaluation of hourly simulation of TropNO₂VCDs with MAX-DOAS measurements in the three sites (a) WD, (b) QKY, and (c) DQS.

posterior emissions were closest to surface observations for NO₂ and O₃ when compared to those using KNMI posterior and prior emissions.

3.3.2. Comparison between Simulated Column Concentrations and MAX-DOAS Observation. The results for all three sites (WD, QKY, and DQS) showed that (Figure 5) the correlation between the simulated concentrations using posterior NO_x emissions and the observed concentrations was significantly improved when compared to the simulated values using prior NO_x emissions. Before the TROPOMI constraint, the R² for NO₂ concentrations was approximately 0.39–0.46, and after the calibration by KNMI and USTC, it increased to approximately 0.58–0.65 and 0.68–0.74 for the posterior and prior emissions, respectively. Before the calibration, the RMSE for NO₂ concentrations was 1.87–2.12 (×10¹⁶ molecules/cm²), and after the calibration by KNMI and USTC, it decreased to 0.95–1.14 (×10¹⁶ molecules/cm²) and 0.69–0.87 (×10¹⁶ molecules/cm²), respectively.

The QKY and DQS sites are located in the city center, and their concentrations are higher than WD, and the correlation is lower than WD. This may be attributed to emissions from vehicles on the road close to the observation sites.⁶⁸ One interesting finding is that different slopes appear in the

simulated TropNO₂VCDs against the MAX-DOAS one for the three periods, which P1 > P3 > P2 (Figure S3). When the concentration of NO₂ is lower, its distribution is closer to the surface, and TROPOMI underestimates NO₂ more obviously, resulting in a smaller slope.⁶⁹ The simulated NO₂ VCDs from the prior emissions were higher than the observed values, and the simulated NO₂ VCDs using the KNMI posterior emissions were lower than those using USTC posterior, which is consistent with TROPOMI observation. Overall, TROPOMI-derived NO_x emissions improved the correlation between NO₂ and O₃ simulation with in situ MAX-DOAS and CNEMC network, and USTC posterior performed lesser bias than KNMI one in the NCP during COVID-19.

3.4. Simulated NO₂ and O₃ Concentration Evaluation

3.4.1. On the Spatial Scale. The constrained NO_x emissions with satellite observations could play an important role in the NO₂ and O₃ simulation. We compared the NO₂ and O₃ concentrations of KNMI posterior, USTC posterior, and prior emissions across the six provinces.

The surface NO₂ concentrations estimated using KNMI and USTC posterior decreased by approximately 41–56 and 36–51%, respectively, when compared to that using prior

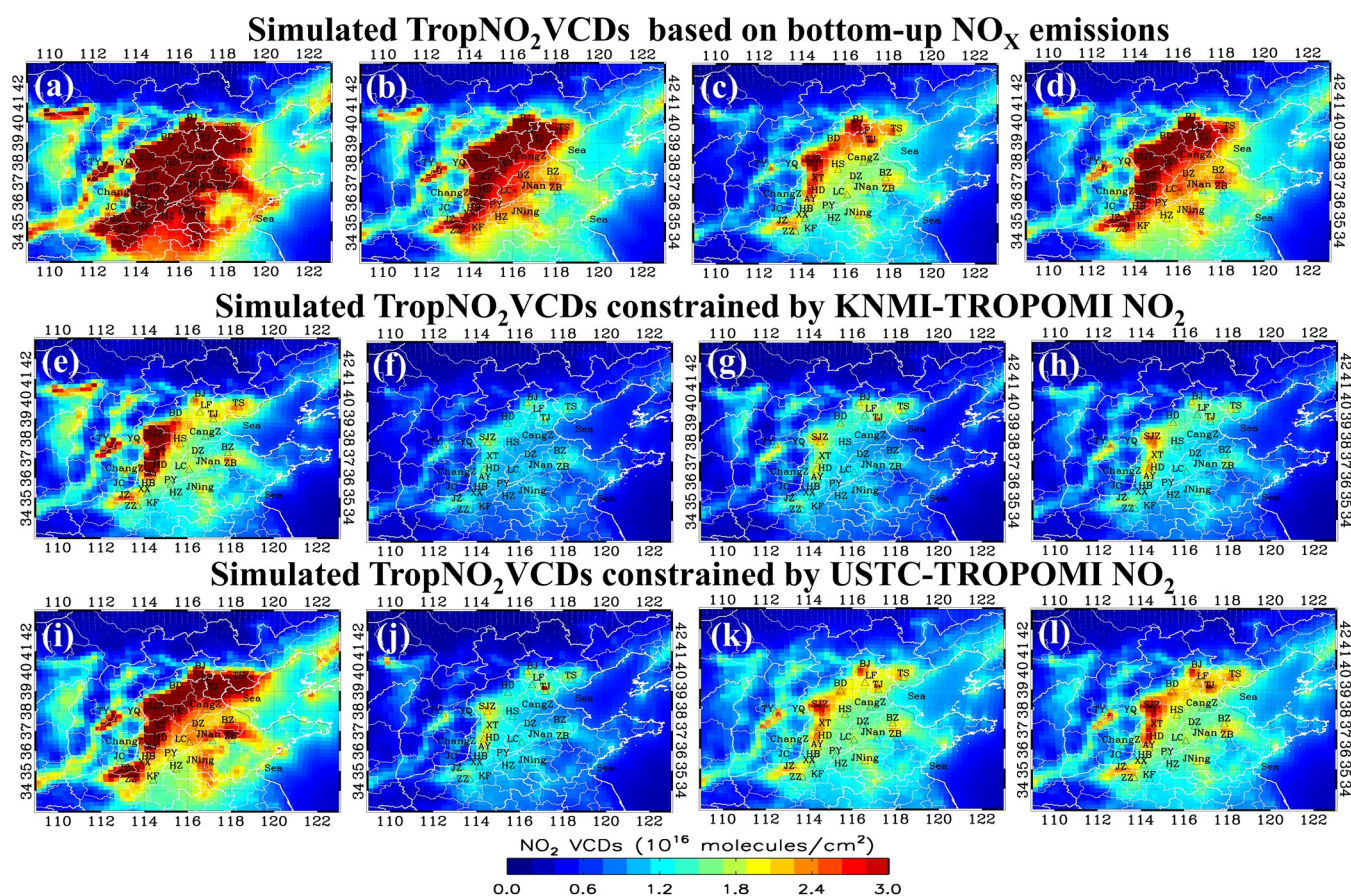


Figure 6. Simulated TropNO₂VCDs based on bottom-up NO_x emissions (a–d), constrained by (e–h) KNMI and (i–l) USTC products. The column panels from left to right represent the average TropNO₂VCD distribution in P1, P2, P3, and the 3-month period, respectively.

emissions; the surface NO₂ concentrations from USTC posterior increased by approximately 9–20% compared to those from KNMI posterior. The TropNO₂VCDs obtained using KNMI and USTC posterior emissions decreased by approximately 36–62 and 30–53%, respectively, when compared to that using prior emissions; the TropNO₂VCDs from USTC posterior increased by approximately 10–25% compared to those from KNMI posterior. The NO₂ surface concentrations and TropNO₂VCDs from USTC posterior were higher than those from KNMI posterior in most cities during the three periods, except for TY in P1, which is consistent with the TROPOMI observation (Figures 6 and S4). In places where key polluting enterprises are concentrated (BJ–TJ–HB region), the impact of the epidemic on the emission concentration of key polluting enterprises varies greatly from P1 to P2 and from P2 to P3.

It is well known that O₃ has a non-linear dependence on its precursors and that NO_x can either decrease or increase O₃ depending on the relative abundance of NO_x to VOCs^{70,71} For this study, in contrast to the change in NO₂ concentration, the surface O₃ concentrations determined using KNMI and USTC posterior increased by approximately 71–82 and 50–65%, respectively, when compared to that using prior emissions; the surface O₃ concentrations from USTC posterior decreased by approximately 6–12% compared to those from KNMI posterior. The tropospheric O₃ VCDs (TropO₃VCDs) using KNMI and USTC posterior emissions increased by approximately 17–28 and 13–21%, respectively, when compared to that using prior emissions; the TropO₃VCDs from USTC

posterior emissions decreased by approximately 3–7% compared to those from KNMI posterior. The O₃ surface concentrations from USTC posterior was lower than those from KNMI posterior in most cities during the three periods, especially 18% lower in P1 (Figures 7 and S5).

3.4.2. On the Temporal Scale. We compared the changes of NO₂ and O₃ concentrations based on KNMI posterior, USTC posterior, and prior emissions for the three periods (Figure 8).

The NO₂ simulation based on the prior did not decrease significantly from P1 to P2 and did not increase but decreased from P2 to P3 (changes in surface concentrations: P2 vs P1 –24%, P3 vs P2 –25%; changes in TropNO₂VCDs: P2 vs P1 –27%, P3 vs P2 –35%). While the simulation after satellite constraints well reproduced the process of NO₂ decreasing from P1 to P2 and then increasing from P2 to P3 (changes in surface concentrations based on KNMI and USTC posterior: P2 vs P1 –44% and –46%, P3 vs P2 +17% and +25%; changes in TropNO₂VCDs based on KNMI and USTC posterior: P2 vs P1 –47% and –50%, P3 vs P2 +30% and +41%). These results are consistent with the recent findings of refs 72 and 73. The decreasing rate of NO₂ concentrations was order by USTC posterior > KNMI posterior > prior during P2 compared to P1 and the increasing rate order by USTC posterior > KNMI posterior during P3 compared to P2.

The O₃ surface concentrations and TropO₃VCDs before and after the adjustments exhibited a continuously increasing trend. The O₃ simulation based on prior increases at similar rates from P1 to P2 and P2 to P3 (changes in surface

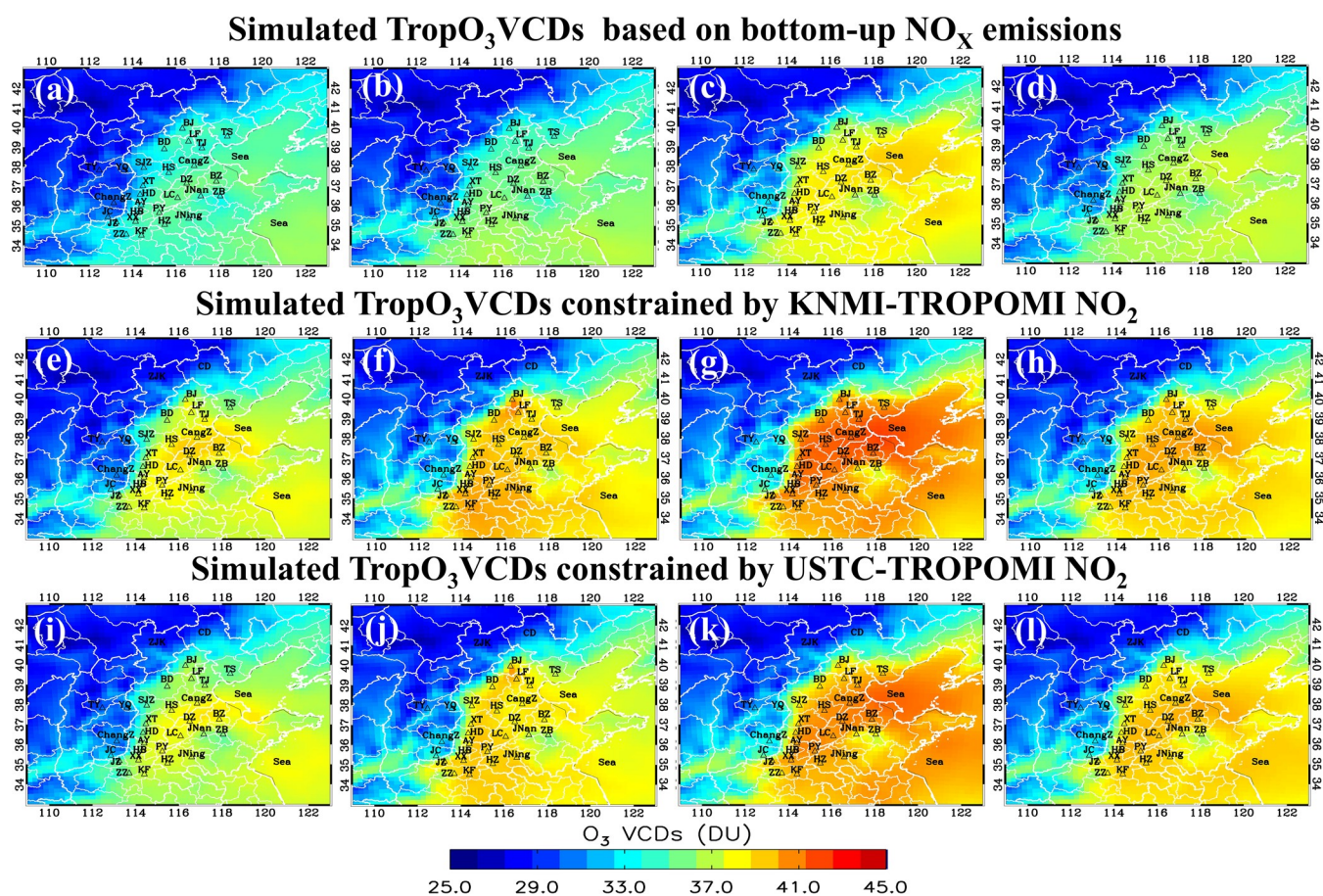


Figure 7. Simulated TropO₃VCDs based on bottom-up NO_x emissions (a–d), constrained by (e–h) KNMI and (i–l) USTC products. The column panels from left to right represent the average TropO₃VCD distribution in P1, P2, P3, and the 3-month period, respectively.

concentrations: P2 vs P1 +37%, P3 vs P2: +41%; changes in TropO₃VCDs: P2 vs P1 +7%, P3 vs P2: +8%). However, the increase rate of O₃ simulation from P1 to P2 after satellite constraint is significantly steeper than that from P2 to P3 (changes in surface concentrations based on KNMI and USTC posterior: P2 vs P1 +66% and +75%, P3 vs P2: +17% and +18%; changes in TropO₃VCDs based on KNMI and USTC posterior: P2 vs P1 +12% and +16%, P3 vs P2: +4% and +6%), caused by the large reduced in NO_x emissions during P2. This finding was supported by precious studies, the O₃ production in urban areas with high NO_x/VOCs ratios is VOCs limited, and reducing NO_x emissions can increase O₃ due to decreased titration of O₃ and radicals.^{74,75} Additionally, above findings indicated that, compared to the simulation based on the other two top-down emissions, the NO₂ and O₃ simulation based on USTC shows the largest variation from P1 to P2 and from P2 to P3.

3.5. Transport Flux in BJ

In addition to local emissions, the transport of pollutants also plays an important role in air quality. Transport flux is strongly influenced by changes in pollutant concentration and wind field and then affects the accumulation or diffusion of local pollutants.^{76,77} The lifetimes of NO₂ and O₃ (~22 d on global average) are long enough for regional transport.⁷⁸ For this reason, the effects of different NO_x emissions on BJ transport flux were evaluated (Table 3). Positive values mean net flux is outflow NO₂ or O₃ from BJ, which represented by outflow from BJ. Negative values mean net flux is inflow NO₂ or O₃ to BJ,

which is represented by the influx of BJ. Compared to the flux from prior simulation, the top-down adjustments showed that the tropospheric NO₂ outflux in all the three periods were decreased significantly (KNMI: −46, −95 and −113%, USTC: −29, −85 and −133%), and the O₃ influx from the surrounding cities were increased slightly (KNMI: 22, 15 and 20%, USTC: 16, 8 and 13%). The NO₂ outflux (2.6 Gg/month) from BJ using prior emissions and turned into NO₂ influx (KNMI: −0.3 Gg/month, USTC: −0.8 Gg/month) from neighboring cities in P3 after satellite constraints, which due to a combination of concentration changes and wind fields. Compared to the model using the KNMI posterior, the revised USTC model showed that the output of NO₂ in BJ was two times (219%) higher in P2 and 1.5 times (147%) higher in P3, whereas the output of O₃ from the surrounding cities to BJ was almost the same (differ by 5–6%) in the three periods.

4. CONCLUSIONS

The outbreak of COVID-19 led to substantial decrease of NO_x emission and air pollutants changes in NCP. Our goals were threefold: (1) quantify the NO_x emission changes, (2) assess how well TROPOMI-adjusted NO₂ and O₃ simulations compare to observations, and (3) investigated the impacts of NO_x emissions on the simulated concentration, variation trend, and transport flux for NO₂ and O₃. Our study revealed significant differences in NO₂ and O₃ simulations constrained by the two TROPOMI retrievals, and USTC posterior have lower bias in the NCP during COVID-19.

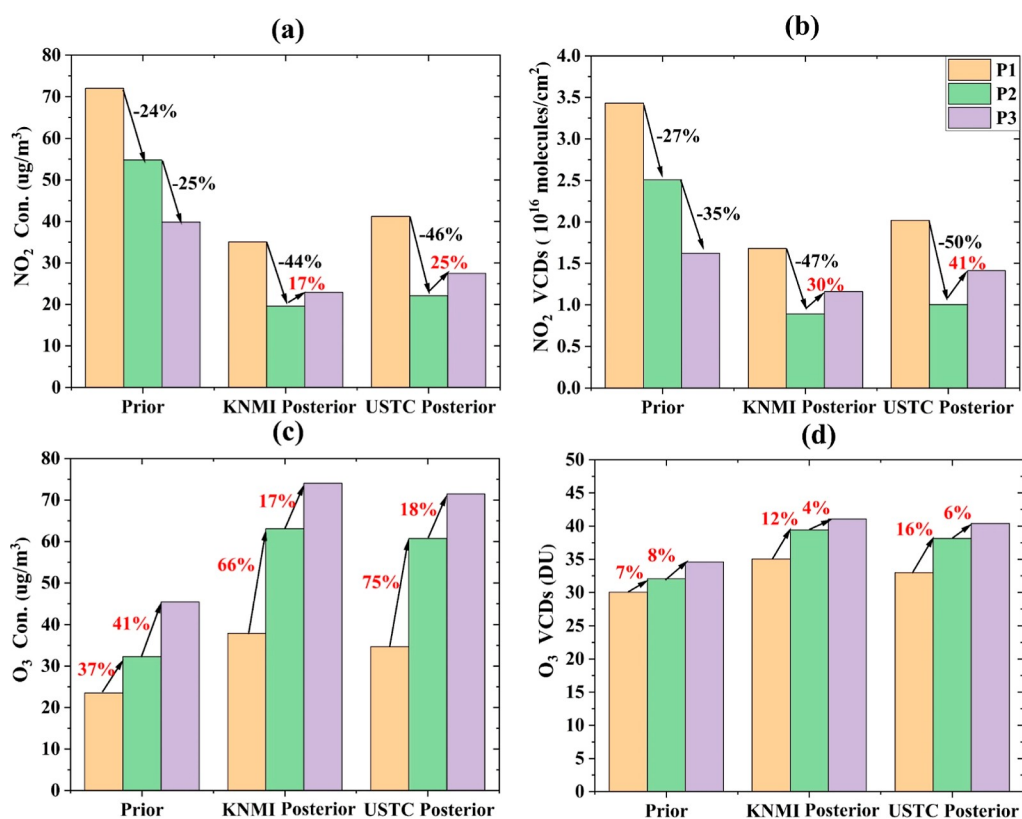


Figure 8. Effects of NO_x emissions on air pollutants simulation over “2 + 26” cities. (a,b) present the regional 0–23 h averaged NO₂ surface concentrations and TropNO₂VCDs; (c,d) are the same as (a,b) expect for O₃.

Table 3. Transport Fluxes of NO₂ and O₃ in BJ during Jan.–Mar., 2020 (Gg/month)

NO ₂ net flux (Gg/month)	prior	KNMI posterior	USTC posterior	KNMI posterior vs prior (%)	USTC posterior vs prior (%)	USTC posterior vs KNMI posterior (%)
	P1	9.6	5.2	6.8	−46	−29
P2	5.8	0.3	0.9	−95	−85	219
P3	2.6	−0.3	−0.8	−113	−133	147
O ₃ net flux (Gg/month)	prior	KNMI posterior	USTC posterior	KNMI posterior vs prior (%)	USTC posterior vs prior (%)	USTC posterior vs KNMI posterior (%)
	P1	−99.6	−121.5	−116.0	22	16
P2	−53.7	−61.4	−58.0	14	8	−6
P3	−96.4	−115.7	−109.1	20	13	−6

From a top-down perspective, we estimated the NO_x emissions using two NO₂ retrievals (KNMI and USTC) from TROPOMI combined with WRF-Chem simulations. The two TROPOMI posterior corrected the positive bias of the bottom-up NO_x emissions (decreased by 18–49 and 4–35%, respectively). Although budgets of averaged NO_x emissions from the USTC posterior were 17–31% larger than the KNMI values, their trends in the three period are well correlated with each other. NO_x emissions in “2 + 26” cities NO_x emissions decreased (KNMI: −27%, USTC: −34%) significantly from P1 to P2 and then increased (USTC: +30%, KNMI: +50%) in P3. Zheng et al.⁷⁹ developed a novel bottom-up approach and found that the monthly NO_x emissions in 2020 over China have changed 1.69 Tg to 1.04 Tg (decreased by 38%) from January to February and then increased to 1.56 Tg (increased by 50%) from February to March, which supported our findings in spite of the different regions between our research. We focused more on “2 + 26” cities in NCP, which captured the attention of the Ministry of Environmental Protection of

China.⁶¹ Our results were also similar with previous research. Zhang et al.⁸⁰ found that NO_x emissions in East China decreased by 50% from P1 to T2 (January 23 to February 9, 2020) and increased by 26% from T2 to T3 (February 10 to March 12, 2020). Zhang et al.³¹ discovered that NO_x emission intensity in China declined by 44.7% from P1 to T2 and increased by 20.3% during the 4 weeks after T2.

As several studies previously have investigated the relation between NO_x and O₃ formation.^{81,82} NO_x assimilation impact tropospheric chemistry, and therefore, improve the estimates of O₃ simulations.^{16,17} Compared to ground-based measurements from MAX-DOAS and CNEMC network over “2 + 26” cities,⁴² modeling with the two posterior NO_x emissions effectively improved the performance of NO₂ and O₃. In addition, modeling simulations using the USTC posterior NO_x emissions exhibited the smallest bias with surface NO₂ and O₃ measurements (KNMI: MREs were −27 and +18%, respectively; USTC: MREs were −15 and +11%, respectively). This is in line with other validation activities that suggest that

KNMI-TROPOMI NO₂ columns are on average some 20–40% lower than measured with independent ground-based measurements.^{37,64} For USTC-TROPOMI retrieval, the main algorithm improvements include the use of local-updated a priori information from the regional chemical transport model, pixel-by-pixel RTM calculations instead of interpolations by a look-up table, and optimized configuration parameters such as instrument slit functions and gas cross sections.^{40,41}

By comparing the changes of NO₂ and O₃ concentrations based on the other two top-down emissions during the three periods, the NO₂ and O₃ simulation based on USTC shows the larger rate of change from P1 to P2 (P2 vs P1: NO₂ surface con. decrease by 46%, TropNO₂VCDs decrease by 50%; O₃ surface con. increase by 75%, TropO₃VCDs increase by 16%) and from P2 to P3 (P3 vs P2: NO₂ surface con. increase by 25%, TropNO₂VCDs increase by 41%; O₃ surface con. increase by 18%, TropO₃VCDs increase by 6%). Similar NO₂ and O₃ changes have been reported in previous studies. According to satellite and surface observations, compared with the period before the lockdown, NO₂ concentrations decreased by ~50% in China during the lockdown period,^{83,84} surface O₃ concentrations in northern and central China increased by ~100%. Zhao et al.⁸⁵ found that Tropospheric Ozone Column over eastern China increased by 10% from pre-lockdown to pre-lockdown period. It was supported by that in the VOC-limited region, reducing NO_x concentrations may cause local increases in O₃.⁸⁶

The NO₂ and O₃ simulations based on different NO_x inventories also influenced the net-flux in BJ, especially on the net-flux of NO₂. For the NO₂ outflux in BJ, the posterior simulations decreased sharply than prior simulations during P2 and P3 (KNMI: –95% and –113%, USTC: –85% and –133%). In addition, BJ outflow NO₂ along with the inflow of O₃ in the first two periods. This is due to the difference in the distribution of NO₂ and O₃ concentrations within the BJ and the surrounding cities. As the areas downwind of large urban areas will experience some O₃ formation due to NO_x outflow.⁸⁷ The obvious difference between USTC and KNMI posteriors appeared in NO₂ outflux, and USTC was 1.5–2 times of KNMI. For O₃ influx, there was little difference. These were due to the different vertical profiles of NO₂ and O₃ concentrations.^{85,88}

Two apparent limitations of this study are as follows: (1) there is only one TROPOMI observation data per day; hence, the NO₂ discrepancies between satellite observation and model simulation at ~13:00 were used to estimate the top-down NO_x emission. However, the diurnal variation of NO_x during COVID-19 varies greatly compared to the prior one, so there are still large discrepancies in diurnal variations between simulation and observation for NO₂ and O₃. Future geostationary satellite observations will provide updated NO_x emissions on an hourly basis, may help us better understand the diurnal variations of NO₂ and O₃ concentrations. (2) Non-methane VOCs (NMVOCs) also play an important role in O₃ formation,^{89,90} and have a significant decline (–37%) over China from January to February, 2020. It has been shown that VOCs and NO_x emissions can affect the production or loss of each other.⁹¹ Meanwhile, we did not consider both NO₂ and NMVOC (e.g. formaldehyde, HCHO) changes in our top-down inversions.^{33,92} Future research can focus on incorporating both species in the top-down method by dealing with the tangled relationship between VOC–NO₂ and NO_x–HCHO.

■ ASSOCIATED CONTENT

SI Supporting Information

The Supporting Information is available free of charge at <https://pubs.acs.org/doi/10.1021/acsenvironau.2c00013>.

Details on the air pollutant flux calculation; comparison of NO₂ and O₃ concentration from simulation and in situ observation; Evaluation of surface NO₂ and O₃ concentration from the prior and TROPOMI posterior simulation; and total NO_x emission budgets during the three periods and relative changes between them (PDF)

■ AUTHOR INFORMATION

Corresponding Authors

Cheng Liu – Key Lab of Environmental Optics & Technology, Anhui Institute of Optics and Fine Mechanics, Chinese Academy of Sciences, Hefei 230031, China; Center for Excellence in Regional Atmospheric Environment, Institute of Urban Environment, Chinese Academy of Sciences, Xiamen 361021, China; Department of Precision Machinery and Precision Instrumentation, University of Science and Technology of China, Hefei 230026, China; Key Laboratory of Precision Scientific Instrumentation of Anhui Higher Education Institutes, University of Science and Technology of China, Hefei 230026, China; orcid.org/0000-0002-3759-9219; Email: chliu81@ustc.edu.cn

Qihou Hu – Key Lab of Environmental Optics & Technology, Anhui Institute of Optics and Fine Mechanics, Chinese Academy of Sciences, Hefei 230031, China; Email: qhhu@aiofm.ac.cn

Authors

Yizhi Zhu – Key Lab of Environmental Optics & Technology, Anhui Institute of Optics and Fine Mechanics, Chinese Academy of Sciences, Hefei 230031, China

Jiahua Teng – China Satellite Application Center for Ecology and Environment, MEE, Beijing 100094, China

Daian You – China Satellite Application Center for Ecology and Environment, MEE, Beijing 100094, China

Chengxin Zhang – Department of Precision Machinery and Precision Instrumentation, University of Science and Technology of China, Hefei 230026, China

Jinping Ou – Key Lab of Environmental Optics & Technology, Anhui Institute of Optics and Fine Mechanics, Chinese Academy of Sciences, Hefei 230031, China

Ting Liu – School of Earth and Space Sciences, University of Science and Technology of China, Hefei 230026, China

Jinan Lin – Key Lab of Environmental Optics & Technology, Anhui Institute of Optics and Fine Mechanics, Chinese Academy of Sciences, Hefei 230031, China

Tianyi Xu – School of Environmental Science and Optoelectronic Technology, University of Science and Technology of China, Hefei 230026, China

Xinhua Hong – School of Environmental Science and Optoelectronic Technology, University of Science and Technology of China, Hefei 230026, China

Complete contact information is available at:

<https://pubs.acs.org/doi/10.1021/acsenvironau.2c00013>

Author Contributions

Y.Z.: conducted a research, designed the experiments, performed the simulation, processed the data, wrote original

draft, and revised the manuscript. C.L.: provided the ideas and financial support and reviewed the manuscript. Q.H.: visualized the model results and verified the conclusions. J.T.: reviewed the manuscript. D.Y.: provided critical reviews pre-publication stage. C.Z.: methodology and provided the TROPOMI NO₂ products. J.O.: reviewed the manuscript. T.L.: validated the model performance and analyzed the study data. J.L.: methodology and provided the MAX-DOAS NO₂ products. T.X.: Validated the model performance. X.H.: Verified the results.

Notes

The authors declare no competing financial interest.

ACKNOWLEDGMENTS

This work was financially supported by the National Key Technology R&D Program of China (2019YFC0214702), the National Natural Science Foundation of China (41775025), the Strategic Priority Research Program of the Chinese Academy of Sciences (no. XDA23020301), the National Natural Science Foundation of China (nos. U21A2027, 41977184, and 41941011), the Key Research and Development Project of Anhui Province (202104i07020002), the Major Projects of High Resolution Earth Observation Systems of National Science and Technology (05-Y30B01-9001-19/20-3), the Youth Innovation Promotion Association of CAS (2021443), and the Young Talent Project of the Center for Excellence in Regional Atmospheric Environment, CAS (CERAE202004).

REFERENCES

- (1) Itahashi, S.; Ge, B.; Sato, K.; Fu, J. S.; Wang, X.; Yamaji, K.; Nagashima, T.; Li, J.; Kajino, M.; Liao, H.; Zhang, M.; Wang, Z.; Li, M.; Kurokawa, J.; Carmichael, G. R.; Wang, Z. MICS-Asia III: overview of model intercomparison and evaluation of acid deposition over Asia. *Atmos. Chem. Phys.* **2020**, *20*, 2667–2693.
- (2) Ge, B.; Itahashi, S.; Sato, K.; Xu, D.; Wang, J.; Fan, F.; Tan, Q.; Fu, J. S.; Wang, X.; Yamaji, K.; Nagashima, T.; Li, J.; Kajino, M.; Liao, H.; Zhang, M.; Wang, Z.; Li, M.; Woo, J.-H.; Kurokawa, J.; Pan, Y.; Wu, Q.; Liu, X.; Wang, Z. Model Inter-Comparison Study for Asia (MICS-Asia) phase III: multimodel comparison of reactive nitrogen deposition over China. *Atmos. Chem. Phys.* **2020**, *20*, 10587–10610.
- (3) Collins, W. J.; Stevenson, D. S.; Johnson, C. E.; Derwent, R. G. Tropospheric ozone in a global-scale three-dimensional Lagrangian model and its response to NO_x emission controls. *J. Atmos. Chem.* **1997**, *26*, 223–274.
- (4) Sillman, S. O₃-NO_x-VOC sensitivity and NO_x-VOC indicators in Paris: Results from models and Atmospheric Pollution Over the Paris Area (ESQUIF) measurements. *J. Geophys. Res.* **2003**, *108*, 8563.
- (5) Frost, G. J.; McKeen, S. A.; Trainer, M.; Ryerson, T. B.; Neuman, J. A.; Roberts, J. M.; Swanson, A.; Holloway, J. S.; Sueper, D. T.; Fortin, T.; Parrish, D. D.; Fehsenfeld, F. C.; Flocke, F.; Peckham, S. E.; Grell, G. A.; Kowal, D.; Cartwright, J.; Auerbach, N.; Habermann, T. Effects of changing power plant NO_x emissions on ozone in the eastern United States: Proof of concept. *J. Geophys. Res.* **2006**, *111*, D12306.
- (6) Choi, Y.; Kim, H.; Tong, D.; Lee, P. Summertime weekly cycles of observed and modeled NO_x and O₃ concentrations as a function of satellite-derived ozone production sensitivity and land use types over the Continental United States. *Atmos. Chem. Phys.* **2012**, *12*, 6291–6307.
- (7) Sillman, S. Some theoretical results concerning O₃-NO_x-VOC chemistry and NO_x-VOC indicators. *J. Geophys. Res.* **2002**, *107*, 4659.
- (8) Sillman, S. The relation between ozone, NO_x and hydrocarbons in urban and polluted rural environments. *Atmos. Environ.* **1999**, *33*, 1821–1845.
- (9) Zhao, Y.; Mao, P.; Zhou, Y.; Yang, Y.; Zhang, J.; Wang, S.; Dong, Y.; Xie, F.; Yu, Y.; Li, W. Improved provincial emission inventory and speciation profiles of anthropogenic non-methane volatile organic compounds: a case study for Jiangsu, China. *Atmos. Chem. Phys.* **2017**, *17*, 7733–7756.
- (10) Zaveri, R. A.; Berkowitz, C. M.; Kleinman, L. I.; Springston, S. R.; Doskey, P. V.; Lonneman, W. A.; Spice, C. W. Ozone production efficiency and NO_x depletion in an urban plume: Interpretation of field observations and implications for evaluating O₃-NO_x-VOC sensitivity. *J. Geophys. Res.* **2003**, *108*, 4436.
- (11) Wang, X.; Yin, S.; Zhang, R.; Yuan, M.; Ying, Q. Assessment of summertime O₃ formation and the O₃-NO_x-VOC sensitivity in Zhengzhou, China using an observation-based model. *Sci. Total Environ.* **2022**, *813*, 152449.
- (12) Jin, X.; Fiore, A.; Boersma, K. F.; Smedt, I. D.; Valin, L. Inferring Changes in Summertime Surface Ozone-NO_x-VOC Chemistry over U.S. Urban Areas from Two Decades of Satellite and Ground-Based Observations. *Environ. Sci. Technol.* **2020**, *54*, 6518–6529.
- (13) Blanchard, C. L.; Shaw, S. L.; Edgerton, E. S.; Schwab, J. J. Emission influences on air pollutant concentrations in New York State: I. ozone. *Atmos. Environ.: X* **2019**, *3*, 100033.
- (14) Yan, Y.; Lin, J.; He, C. Ozone trends over the United States at different times of day. *Atmos. Chem. Phys.* **2018**, *18*, 1185–1202.
- (15) Verstraeten, W. W.; Neu, J. L.; Williams, J. E.; Bowman, K. W.; Worden, J. R.; Boersma, K. F. Rapid increases in tropospheric ozone production and export from China. *Nat. Geosci.* **2015**, *8*, 690–695.
- (16) Visser, A. J.; Boersma, K. F.; Ganzeveld, L. N.; Krol, M. C. European NO_x emissions in WRF-Chem derived from OMI: impacts on summertime surface ozone. *Atmos. Chem. Phys.* **2019**, *19*, 11821–11841.
- (17) Qu, Z.; Henze, D. K.; Cooper, O. R.; Neu, J. L. Impacts of global NO_x inversions on NO₂ and ozone simulations. *Atmos. Chem. Phys.* **2020**, *20*, 13109–13130.
- (18) Choi, Y. The impact of satellite-adjusted NO_x emissions on simulated NO_x and O₃ discrepancies in the urban and outflow areas of the Pacific and Lower Middle US. *Atmos. Chem. Phys.* **2014**, *14*, 675–690.
- (19) Zhao, Y.; Xia, Y.; Zhou, Y. Assessment of a high-resolution NO_x emission inventory using satellite observations: A case study of southern Jiangsu, China. *Atmos. Environ.* **2018**, *190*, 135–145.
- (20) Li, M.; Liu, H.; Geng, G.; Hong, C.; Liu, F.; Song, Y.; Tong, D.; Zheng, B.; Cui, H.; Man, H.; Zhang, Q.; He, K. Anthropogenic emission inventories in China: a review. *Natl. Sci. Rev.* **2017**, *4*, 834–866.
- (21) Martin, R. V. Global inventory of nitrogen oxide emissions constrained by space-based observations of NO₂ columns. *J. Geophys. Res.* **2003**, *108*, 4537.
- (22) Wang, S. W.; Zhang, Q.; Streets, D. G.; He, K. B.; Martin, R. V.; Lamsal, L. N.; Chen, D.; Lei, Y.; Lu, Z. Growth in NO_x emissions from power plants in China: bottom-up estimates and satellite observations. *Atmos. Chem. Phys.* **2012**, *12*, 4429–4447.
- (23) Tan, W.; Zhao, S.; Liu, C.; Chan, K. L.; Xie, Z.; Zhu, Y.; Su, W.; Zhang, C.; Liu, H.; Xing, C.; Liu, J. Estimation of winter time NO_x emissions in Hefei, a typical inland city of China, using mobile MAX-DOAS observations. *Atmos. Environ.* **2019**, *200*, 228–242.
- (24) Liu, X.; Gao, X.; Wu, X.; Yu, W.; Chen, L.; Ni, R.; Zhao, Y.; Duan, H.; Zhao, F.; Chen, L.; Gao, S.; Xu, K.; Lin, J.; Ku, A. Y. Updated Hourly Emissions Factors for Chinese Power Plants Showing the Impact of Widespread Ultralow Emissions Technology Deployment. *Environ. Sci. Technol.* **2019**, *53*, 2570–2578.
- (25) Martin, R. V.; Sioris, C. E.; Chance, K.; Ryerson, T. B.; Bertram, T. H.; Wooldridge, P. J.; Cohen, R. C.; Neuman, J. A.; Swanson, A.; Flocke, F. M. Evaluation of space-based constraints on global nitrogen oxide emissions with regional aircraft measurements over and downwind of eastern North America. *J. Geophys. Res.* **2006**, *111*, D15308.

- (26) Jin, X.; Zhu, Q.; Cohen, R. C. Direct estimates of biomass burning NO_x emissions and lifetimes using daily observations from TROPOMI. *Atmos. Chem. Phys.* **2021**, *21*, 15569–15587.
- (27) Qu, Z.; Jacob, D. J.; Silvern, R. F.; Shah, V.; Campbell, P. C.; Valin, L. C.; Murray, L. T. US COVID-19 Shutdown Demonstrates Importance of Background NO₂ in Inferring NO_x Emissions From Satellite NO₂ Observations. *Geophys. Res. Lett.* **2021**, *48*, No. e2021GL092783.
- (28) Souri, A. H.; Choi, Y.; Jeon, W.; Li, X.; Pan, S.; Diao, L.; Westenbarger, D. A. Constraining NO_x emissions using satellite NO₂ measurements during 2013 DISCOVER-AQ Texas campaign. *Atmos. Environ.* **2016**, *131*, 371–381.
- (29) Kim, S. W.; Heckel, A.; Frost, G. J.; Richter, A.; Gleason, J.; Burrows, J. P.; McKeen, S.; Hsie, E. Y.; Granier, C.; Trainer, M. NO₂ columns in the western United States observed from space and simulated by a regional chemistry model and their implications for NO_x emissions. *J. Geophys. Res.* **2009**, *114*, D11301.
- (30) Yang, Y.; Zhao, Y.; Zhang, L.; Zhang, J.; Huang, X.; Zhao, X.; Zhang, Y.; Xi, M.; Lu, Y. Improvement of the satellite-derived NO_x emissions on air quality modeling and its effect on ozone and secondary inorganic aerosol formation in the Yangtze River Delta, China. *Atmos. Chem. Phys.* **2021**, *21*, 1191–1209.
- (31) Zhang, Q.; Pan, Y.; He, Y.; Walters, W. W.; Ni, Q.; Liu, X.; Xu, G.; Shao, J.; Jiang, C. Substantial nitrogen oxides emission reduction from China due to COVID-19 and its impact on surface ozone and aerosol pollution. *Sci. Total Environ.* **2021**, *753*, 142238.
- (32) Zheng, F.; Yu, T.; Cheng, T.; Gu, X.; Guo, H. Intercomparison of tropospheric nitrogen dioxide retrieved from Ozone Monitoring Instrument over China. *Atmos. Pollut. Res.* **2014**, *5*, 686–695.
- (33) Qu, Z.; Henze, D. K.; Capps, S. L.; Wang, Y.; Xu, X.; Wang, J.; Keller, M. Monthly top-down NO_x emissions for China (2005–2012): A hybrid inversion method and trend analysis: A hybrid inversion method and trend analysis. *J. Geophys. Res.: Atmos.* **2017**, *122*, 4600–4625.
- (34) Zhu, Y.; Hu, Q.; Gao, M.; Zhao, C.; Zhang, C.; Liu, T.; Tian, Y.; Yan, L.; Su, W.; Hong, X.; Liu, C. Quantifying Contributions of Local Emissions and Regional Transport to NO_x in Beijing Using TROPOMI Constrained WRF-Chem Simulation. *Remote Sens.* **2021**, *13*, 1798–1815.
- (35) Zaveri, R. A.; Peters, L. K. A new lumped structure photochemical mechanism for large-scale applications. *J. Geophys. Res.: Atmos.* **1999**, *104*, 30387–30415.
- (36) Zaveri, R. A.; Easter, R. C.; Fast, J. D.; Peters, L. K. Model for Simulating Aerosol Interactions and Chemistry (MOSAIC). *J. Geophys. Res.* **2008**, *113*, D13204.
- (37) Griffin, D.; Zhao, X.; McLinden, C. A.; Boersma, F.; Bourassa, A.; Dammers, E.; Degenstein, D.; Eskes, H.; Fehr, L.; Fioletov, V.; Hayden, K.; Kharol, S. K.; Li, S. M.; Makar, P.; Martin, R. V.; Mihele, C.; Mittermeier, R. L.; Krotkov, N.; Snee, M.; Lamsal, L. N.; Linden, M. t.; Geffen, J. v.; Veefkind, P.; Wolde, M. High-Resolution Mapping of Nitrogen Dioxide With TROPOMI: First Results and Validation Over the Canadian Oil Sands. *Geophys. Res. Lett.* **2019**, *46*, 1049–1060.
- (38) Liu, J. Mapping high resolution national daily NO₂ exposure across mainland China using an ensemble algorithm. *Environ. Pollut.* **2021**, *279*, 116932.
- (39) van Geffen, J.; Boersma, K. F.; Eskes, H.; Snee, M.; ter Linden, M.; Zara, M.; Veefkind, J. P. SSP TROPOMI NO₂ slant column retrieval: method, stability, uncertainties and comparisons with OMI. *Atmos. Meas. Tech.* **2020**, *13*, 1315–1335.
- (40) Zhang, C.; Liu, C.; Hu, Q.; Cai, Z.; Su, W.; Xia, C.; Zhu, Y.; Wang, S.; Liu, J. Satellite UV-Vis spectroscopy: implications for air quality trends and their driving forces in China during 2005–2017. *Light: Sci. Appl.* **2019**, *8*, 100.
- (41) Liu, C.; Liu, X.; Kowalewski, M. G.; Janz, S. J.; González Abad, G.; Pickering, K. E.; Chance, K.; Lamsal, L. N. Characterization and verification of ACAM slit functions for trace-gas retrievals during the 2011 DISCOVER-AQ flight campaign. *Atmos. Meas. Tech.* **2015**, *8*, 751–759.
- (42) Tan, W.; Liu, C.; Wang, S.; Xing, C.; Su, W.; Zhang, C.; Xia, C.; Liu, H.; Cai, Z.; Liu, J. Tropospheric NO₂, SO₂, and HCHO over the East China Sea, using ship-based MAX-DOAS observations and comparison with OMI and OMPS satellite data. *Atmos. Chem. Phys.* **2018**, *18*, 15387–15402.
- (43) Su, W.; Liu, C.; Chan, K. L.; Hu, Q.; Liu, H.; Ji, X.; Zhu, Y.; Liu, T.; Zhang, C.; Chen, Y.; Liu, J. An improved TROPOMI tropospheric HCHO retrieval over China. *Atmos. Meas. Tech.* **2020**, *13*, 6271–6292.
- (44) Fayt, C.; De Smedt, I.; Letocart, V.; Merlaud, A.; Pinardi, G.; Van Roozendaal, M.; Roozendaal, M. QDOAS Software user manual. *Belg. Inst. Space Aeron. Bruss. Belg.* **2011**, *1*, 1–17.
- (45) Zara, M.; Boersma, K. F.; De Smedt, I.; Richter, A.; Peters, E.; van Geffen, J. H. G. M.; Beirle, S.; Wagner, T.; Van Roozendaal, M.; Marchenko, S.; Lamsal, L. N.; Eskes, H. J. Improved slant column density retrieval of nitrogen dioxide and formaldehyde for OMI and GOME-2A from QA4ECV: intercomparison, uncertainty characterisation, and trends. *Atmos. Meas. Tech.* **2018**, *11*, 4033–4058.
- (46) Spurr, R. J. D. VLIDORT: A linearized pseudo-spherical vector discrete ordinate radiative transfer code for forward model and retrieval studies in multilayer multiple scattering media. *J. Quant. Spectrosc. Radiat. Transfer* **2006**, *102*, 316–342.
- (47) Goldberg, D. L.; Lamsal, L. N.; Loughner, C. P.; Swartz, W. H.; Lu, Z.; Streets, D. G. A high-resolution and observationally constrained OMI NO₂ satellite retrieval. *Atmos. Chem. Phys.* **2017**, *17*, 11403–11421.
- (48) Lamsal, L. N.; Krotkov, N. A.; Vasilkov, A.; Marchenko, S.; Qin, W.; Yang, E.-S.; Fasnacht, Z.; Joiner, J.; Choi, S.; Haffner, D.; Swartz, W. H.; Fisher, B.; Bucsel, E. Ozone Monitoring Instrument (OMI) Aura nitrogen dioxide standard product version 4.0 with improved surface and cloud treatments. *Atmos. Meas. Tech.* **2021**, *14*, 455–479.
- (49) Beirle, S.; Hörmann, C.; Jöckel, P.; Liu, S.; Penning de Vries, M.; Pozzer, A.; Sihler, H.; Valks, P.; Wagner, T. The STRatospheric Estimation Algorithm from Mainz (STREAM): estimating stratospheric NO₂ from nadir-viewing satellites by weighted convolution. *Atmos. Meas. Tech.* **2016**, *9*, 2753–2779.
- (50) Zhang, C.; Liu, C.; Chan, K. L.; Hu, Q.; Liu, H.; Li, B.; Xing, C.; Tan, W.; Zhou, H.; Si, F.; Liu, J. First observation of tropospheric nitrogen dioxide from the Environmental Trace Gases Monitoring Instrument onboard the GaoFen-5 satellite. *Light: Sci. Appl.* **2020**, *9*, 66.
- (51) Wood, S. N. Stable and Efficient Multiple Smoothing Parameter Estimation for Generalized Additive Models. *J. Am. Stat. Assoc.* **2004**, *99*, 673–686.
- (52) Boersma, K. F.; Eskes, H. J.; Richter, A.; De Smedt, I.; Lorente, A.; Beirle, S.; van Geffen, J. H. G. M.; Zara, M.; Peters, E.; Van Roozendaal, M.; Wagner, T.; Maasakkers, J. D.; van der A, R. J.; Nightingale, J.; De Rudder, A.; Irie, H.; Pinardi, G.; Lambert, J.-C.; Compernelle, S. C. Improving algorithms and uncertainty estimates for satellite NO₂ retrievals: results from the quality assurance for the essential climate variables (QA4ECV) project. *Atmos. Meas. Tech.* **2018**, *11*, 6651–6678.
- (53) Williams, J. E.; Boersma, K. F.; Le Sager, P.; Verstraeten, W. W. The high-resolution version of TMS-MP for optimized satellite retrievals: description and validation. *Geosci. Model Dev.* **2017**, *10*, 721–750.
- (54) Lamsal, L. N.; Martin, R. V.; Padmanabhan, A.; van Donkelaar, A.; Zhang, Q.; Sioris, C. E.; Chance, K.; Kurosu, T. P.; Newchurch, M. J. Application of satellite observations for timely updates to global anthropogenic NO_x emission inventories. *Geophys. Res. Lett.* **2011**, *38*, L05810.
- (55) Vinken, G. C. M.; Boersma, K. F.; Maasakkers, J. D.; Adon, M.; Martin, R. V. Worldwide biogenic soil NO_x emissions inferred from OMI NO₂ observations. *Atmos. Chem. Phys.* **2014**, *14*, 10363–10381.
- (56) Zhao, C.; Wang, Y. Assimilated inversion of NO_x emissions over east Asia using OMI NO₂ column measurements. *Geophys. Res. Lett.* **2009**, *36*, L06805.
- (57) Lorente, A.; Boersma, K. F.; Eskes, H. J.; Veefkind, J. P.; van Geffen, J. H. G. M.; de Zeeuw, M. B.; Denier van der Gon, H. A. C.;

- Beirle, S.; Krol, M. C. Quantification of nitrogen oxides emissions from build-up of pollution over Paris with TROPOMI. *Sci. Rep.* **2019**, *9*, 20033.
- (58) Cambaliza, M. O. L.; Shepson, P. B.; Caulton, D. R.; Stirm, B.; Samarov, D.; Gurney, K. R.; Turnbull, J.; Davis, K. J.; Possolo, A.; Karion, A.; Sweeney, C.; Moser, B.; Hendricks, A.; Lauvaux, T.; Mays, K.; Whetstone, J.; Huang, J.; Razlivanov, L.; Miles, N. L.; Richardson, S. J. Assessment of uncertainties of an aircraft-based mass balance approach for quantifying urban greenhouse gas emissions. *Atmos. Chem. Phys.* **2014**, *14*, 9029–9050.
- (59) Hong, Q.; Liu, C.; Chan, K. L.; Hu, Q.; Xie, Z.; Liu, H.; Si, F.; Liu, J. Ship-based MAX-DOAS measurements of tropospheric NO₂, SO₂, and HCHO distribution along the Yangtze River. *Atmos. Chem. Phys.* **2018**, *18*, 5931–5951.
- (60) Wang, L. T.; Wei, Z.; Yang, J.; Zhang, Y.; Zhang, F. F.; Su, J.; Meng, C. C.; Zhang, Q. The 2013 severe haze over southern Hebei, China: model evaluation, source apportionment, and policy implications. *Atmos. Chem. Phys.* **2014**, *14*, 3151–3173.
- (61) Qi, M.; Wang, L.; Ma, S.; Zhao, L.; Lu, X.; Liu, Y.; Zhang, Y.; Tan, J.; Liu, Z.; Zhao, S.; Wang, Q.; Xu, R. Evaluation of PM_{2.5} fluxes in the “2+26” cities: Transport pathways and intercity contributions. *Atmos. Pollut. Res.* **2021**, *12*, 101048.
- (62) Chang, X.; Wang, S.; Zhao, B.; Cai, S.; Hao, J. Assessment of inter-city transport of particulate matter in the Beijing–Tianjin–Hebei region. *Atmos. Chem. Phys.* **2018**, *18*, 4843–4858.
- (63) Lu, X.; Hong, J.; Zhang, L.; Cooper, O. R.; Schultz, M. G.; Xu, X.; Wang, T.; Gao, M.; Zhao, Y.; Zhang, Y. Severe surface ozone pollution in China: a global perspective. *Environ. Sci. Technol. Lett.* **2018**, *5*, 487–494.
- (64) Verhoelst, T.; Compernelle, S.; Pinardi, G.; Lambert, J.-C.; Eskes, H. J.; Eichmann, K.-U.; Fjæraa, A. M.; Granville, J.; Niemeijer, S.; Cede, A.; Tiefengraber, M.; Hendrick, F.; Pazmiño, A.; Bais, A.; Bazureau, A.; Boersma, K. F.; Bogner, K.; Dehn, A.; Donner, S.; Elokhev, A.; Gebetsberger, M.; Goutail, F.; Grutter de la Mora, M.; Gruzdev, A.; Gratsea, M.; Hansen, G. H.; Irie, H.; Jepsen, N.; Kanaya, Y.; Karagiozidis, D.; Kivi, R.; Kreher, K.; Levelt, P. F.; Liu, C.; Müller, M.; Navarro Comas, M.; PETERS, A. J. M.; Pommereau, J.-P.; Portafax, T.; Prados-Roman, C.; Puentedura, O.; Querel, R.; Remmers, J.; Richter, A.; Rimmer, J.; Rivera Cárdenas, C.; Saavedra de Miguel, L.; Sinyakov, V. P.; Stremme, W.; Strong, K.; Van Roozendaal, M.; Veefkind, J. P.; Wagner, T.; Wittrock, F.; Yela González, M.; Zehner, C. Ground-based validation of the Copernicus Sentinel-5P TROPOMI NO₂ measurements with the NDACC ZSL-DOAS, MAX-DOAS and Pandora global networks. *Atmos. Meas. Tech.* **2021**, *14*, 481–510.
- (65) Judd, L. M.; Al-Saadi, J. A.; Szykman, J. J.; Valin, L. C.; Janz, S. J.; Kowalewski, M. G.; Eskes, H. J.; Veefkind, J. P.; Cede, A.; Mueller, M.; Gebetsberger, M.; Swap, R.; Pierce, R. B.; Nowlan, C. R.; Abad, G. G.; Nehrir, A.; Williams, D. Evaluating Sentinel-5P TROPOMI tropospheric NO₂ column densities with airborne and Pandora spectrometers near New York City and Long Island Sound. *Atmos. Meas. Tech.* **2020**, *13*, 6113–6140.
- (66) He, C.; Yang, L.; Cai, B.; Ruan, Q.; Hong, S.; Wang, Z. Impacts of the COVID-19 event on the NO_x emissions of key polluting enterprises in China. *Appl. Energy* **2021**, *281*, 116042.
- (67) Feng, S.; Jiang, F.; Wang, H.; Wang, H.; Ju, W.; Shen, Y.; Zheng, Y.; Wu, Z.; Ding, A. NO_x Emission Changes Over China During the COVID-19 Epidemic Inferred From Surface NO₂ Observations. *Geophys. Res. Lett.* **2020**, *47*, No. e2020GL090080.
- (68) Xing, C.; Liu, C.; Wang, S.; Chan, K. L.; Gao, Y.; Huang, X.; Su, W.; Zhang, C.; Dong, Y.; Fan, G.; Zhang, T.; Chen, Z.; Hu, Q.; Su, H.; Xie, Z.; Liu, J. Observations of the vertical distributions of summertime atmospheric pollutants and the corresponding ozone production in Shanghai, China. *Atmos. Chem. Phys.* **2017**, *17*, 14275–14289.
- (69) van Geffen, J. H. G. M.; Boersma, K. F.; Veefkind, J. P. TROPOMI ATBD of the Total and Tropospheric NO₂ Data Products. CI-7430-ATBD, 2019.
- (70) Atkinson, R. Atmospheric chemistry of VOCs and NO_x. *Atmos. Environ.* **2013**, *34*, 2063–2101.
- (71) Wang, T.; Xue, L.; Brimblecombe, P.; Lam, Y. F.; Li, L.; Zhang, L. Ozone pollution in China: A review of concentrations, meteorological influences, chemical precursors, and effects. *Sci. Total Environ.* **2017**, *575*, 1582–1596.
- (72) Wang, P.; Chen, K.; Zhu, S.; Wang, P.; Zhang, H. Severe air pollution events not avoided by reduced anthropogenic activities during COVID-19 outbreak. *Resour., Conserv. Recycl.* **2020**, *158*, 104814.
- (73) Huang, X.; Ding, A.; Gao, J.; Zheng, B.; Zhou, D.; Qi, X.; Tang, R.; Wang, J.; Ren, C.; Nie, W.; Chi, X.; Xu, Z.; Chen, L.; Li, Y.; Che, F.; Pang, N.; Wang, H.; Tong, D.; Qin, W.; Cheng, W.; Liu, W.; Fu, Q.; Liu, B.; Chai, F.; Davis, S. J.; Zhang, Q.; He, K. Enhanced secondary pollution offset reduction of primary emissions during COVID-19 lockdown in China. *Natl. Sci. Rev.* **2021**, *8*, nwaal37.
- (74) Liu, Y.; Wang, T.; Stavrou, T.; Elguindi, N.; Doumbia, T.; Granier, C.; Bouarar, I.; Gaubert, B.; Brasseur, G. P. Diverse response of surface ozone to COVID-19 lockdown in China. *Sci. Total Environ.* **2021**, *789*, 147739.
- (75) Xing, J.; Ding, D.; Wang, S.; Zhao, B.; Jang, C.; Wu, W.; Zhang, F.; Zhu, Y.; Hao, J. Quantification of the enhanced effectiveness of NO_x control from simultaneous reductions of VOC and NH₃ for reducing air pollution in the Beijing-Tianjin-Hebei region, China. *Atmos. Chem. Phys.* **2018**, *18*, 7799–7814.
- (76) Qu, Z.; Wu, D.; Henze, D. K.; Li, Y.; Sonenberg, M.; Mao, F. Transboundary transport of ozone pollution to a US border region: A case study of Yuma. *Environ. Pollut.* **2021**, *273*, 116421.
- (77) Feng, T.; Zhou, W.; Wu, S.; Niu, Z.; Cheng, P.; Xiong, X.; Li, G. High-resolution simulation of wintertime fossil fuel CO₂ in Beijing, China: Characteristics, sources, and regional transport. *Atmos. Environ.* **2019**, *198*, 226–235.
- (78) Gaudel, A.; Clerbaux, C.; Foret, G.; Liu, J.; Cooper, O. R.; Hassler, B. Tropospheric Ozone Assessment Report: Present-day distribution and trends of tropospheric ozone relevant to climate and global atmospheric chemistry model evaluation. *Elem. Sci. Anthropocene* **2018**, *6*, 39.
- (79) Zheng, B.; Zhang, Q.; Geng, G.; Chen, C.; Shi, Q.; Cui, M.; Lei, Y.; He, K. Changes in China’s anthropogenic emissions and air quality during the COVID-19 pandemic in 2020. *Earth Syst. Sci. Data* **2021**, *13*, 2895–2907.
- (80) Zhang, R.; Zhang, Y.; Lin, H.; Feng, X.; Fu, T.-M.; Wang, Y. NO_x Emission Reduction and Recovery during COVID-19 in East China. *Atmosphere* **2020**, *11*, 433.
- (81) Monks, P. S.; Archibald, A. T.; Colette, A.; Cooper, O.; Coyle, M.; Derwent, R.; Fowler, D.; Granier, C.; Law, K. S.; Mills, G. E.; Stevenson, D. S.; Tarasova, O.; Thouret, V.; von Schneidemesser, E.; Sommariva, R.; Wild, O.; Williams, M. L. Tropospheric ozone and its precursors from the urban to the global scale from air quality to short-lived climate forcer. *Atmos. Chem. Phys.* **2015**, *15*, 8889–8973.
- (82) Su, W.; Liu, C.; Hu, Q.; Fan, G.; Xie, Z.; Huang, X.; Zhang, T.; Chen, Z.; Dong, Y.; Ji, X.; Liu, H.; Wang, Z.; Liu, J. Characterization of ozone in the lower troposphere during the 2016 G20 conference in Hangzhou. *Sci. Rep.* **2017**, *7*, 17368.
- (83) Liu, F.; Page, A.; Strode, S. A.; Yoshida, Y.; Choi, S.; Zheng, B.; Lamsal, L. N.; Li, C.; Krotkov, N. A.; Eskes, H.; van der A, R.; Veefkind, P.; Levelt, P. F.; Hauser, O. P.; Joiner, J. Abrupt decline in tropospheric nitrogen dioxide over China after the outbreak of COVID-19. *Sci. Adv.* **2020**, *6*, No. eabc2992.
- (84) Ghahremanloo, M.; Lops, Y.; Choi, Y.; Mousavinezhad, S. Impact of the COVID-19 outbreak on air pollution levels in East Asia. *Sci. Total Environ.* **2021**, *754*, 142226.
- (85) Zhao, F.; Liu, C.; Cai, Z.; Liu, X.; Bak, J.; Kim, J.; Hu, Q.; Xia, C.; Zhang, C.; Sun, Y.; Wang, W.; Liu, J. Ozone profile retrievals from TROPOMI: Implication for the variation of tropospheric ozone during the outbreak of COVID-19 in China. *Sci. Total Environ.* **2021**, *764*, 142886.

(86) Simon, H.; Reff, A.; Wells, B.; Xing, J.; Frank, N. Ozone trends across the United States over a period of decreasing NO_x and VOC emissions. *Environ. Sci. Technol.* **2015**, *49*, 186–195.

(87) Koplitz, S.; Simon, H.; Henderson, B.; Liljegren, J.; Tonnesen, G.; Whitehill, A.; Wells, B. *Changes in Ozone Chemical Sensitivity in the United States from 2007 to 2016*; ACS Environmental Au, 2021.

(88) Pickering, K. E.; Bucsela, E.; Allen, D.; Ring, A.; Holzworth, R.; Krotkov, N. Estimates of lightning NO_x production based on OMI NO₂ observations over the Gulf of Mexico. *J. Geophys. Res.: Atmos.* **2016**, *121*, 8668–8691.

(89) Simayi, M.; Hao, Y.; Li, J.; Wu, R.; Shi, Y.; Xi, Z.; Zhou, Y.; Xie, S. Establishment of county-level emission inventory for industrial NMVOCs in China and spatial-temporal characteristics for 2010–2016. *Atmos. Environ.* **2019**, *211*, 194–203.

(90) Mondal, A.; Saharan, U. S.; Arya, R.; Yadav, L.; Ahlawat, S.; Jangirh, R.; Kotnala, G.; Choudhary, N.; Banoo, R.; Rai, A.; Yadav, P.; Rani, M.; Lal, S.; Stewart, G. J.; Nelson, B. S.; Acton, W. J. F.; Vaughan, A. R.; Hamilton, J. F.; Hopkins, J. R.; Hewitt, C. N.; Sahu, L. K.; Tripathi, N.; Sharma, S. K.; Mandal, T. K. Non-methane volatile organic compounds emitted from domestic fuels in Delhi: Emission factors and total city-wide emissions. *Atmos. Environ.: X* **2021**, *11*, 100127.

(91) Sourì, A. H.; Nowlan, C. R.; González Abad, G.; Zhu, L.; Blake, D. R.; Fried, A.; Weinheimer, A. J.; Wisthaler, A.; Woo, J.-H.; Zhang, Q.; Chan Miller, C. E.; Liu, X.; Chance, K. An inversion of NO_x and non-methane volatile organic compound (NMVOC) emissions using satellite observations during the KORUS-AQ campaign and implications for surface ozone over East Asia. *Atmos. Chem. Phys.* **2020**, *20*, 9837–9854.

(92) Barkley, M. P.; Smedt, I. D.; Van Roozendaal, M.; Kurosu, T. P.; Chance, K.; Arneth, A.; Hagberg, D.; Guenther, A.; Paulot, F.; Marais, E.; Mao, J. Top-down isoprene emissions over tropical South America inferred from SCIAMACHY and OMI formaldehyde columns. *J. Geophys. Res.: Atmos.* **2013**, *118*, 6849–6868.